Ultramicroscopy 234 (2022) 113477

Contents lists available at ScienceDirect

Ultramicroscopy

journal homepage: www.elsevier.com/locate/ultramic

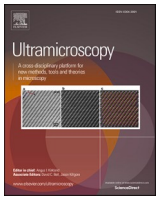

A method for a column-by-column EELS quantification of barium lanthanum ferrate

Judith Lammer [a,*], Christian Berger [b], Stefan Löffler [c], Daniel Knez [a], Paolo Longo [d], Gerald Kothleitner [a], Ferdinand Hofer [a], Georg Haberfehlner [a], Edith Bucher [b], Werner Sitte [b], Werner Grogger [a]

[a] Institute of Electron Microscopy and Nanoanalysis (FELMI), Graz University of Technology & Graz Centre for Electron Microscopy (ZFE), Steyrergasse 17, 8010 Graz, Austria
[b] Chair of Physical Chemistry, Montanuniversitaet Leoben, Franz-Josef-Straße 18, 8700 Leoben, Austria
[c] University Service Centre for Transmission Electron Microscopy (USTEM), TU Wien, Wiedner Hauptstraße 8-10, 1040 Vienna, Austria
[d] Gatan Inc., 5794W Las Positas Blvd, Pleasanton, CA 94588, USA

ARTICLE INFO

Keywords:
EELS quantification
High-resolution STEM
Second order Ruddlesden-Popper phase
Barium lanthanum ferrate
Inelastic multislice simulations

ABSTRACT

High-resolution STEM-EELS provides information about the composition of crystalline materials at the atomic scale, though a reliable quantitative chemical analysis is often hampered by zone axis conditions, where neighbouring atomic column intensities contribute to the signal at the probe position. In this work, we present a procedure to determine the concentration of two elements within equivalent atomic columns from EELS elemental maps – in our case barium and lanthanum within the A-sites of $Ba_{1.1}La_{1.9}Fe_2O_7$, a second order Ruddlesden-Popper phase. We took advantage of the large changes in the elemental distribution from column to column and introduced a technique, which substitutes inelastic scattering cross sections during the quantification step by using parameters obtained from the actual experiment. We considered channelling / de-channelling effects via inelastic multislice simulations and were thereby able to count occupancies in each atomic column. The EELS quantification results were then used as prior information during the Rietveld refinement in XRD measurements in order to differentiate between barium and lanthanum.

1. Introduction

Scanning transmission electron microscopy (STEM), especially in combination with electron energy loss spectroscopy (EELS) and energy-dispersive X-ray spectroscopy (EDXS), is a key tool in nano-characterization, allowing to spatially visualize and map out chemical information at the atomic scale. Initially, this was made possible by the introduction of aberration corrected electron microscopes [1–5], highly sensitive large angle SDD EDXS detectors [6,7], as well as fast direct electron detection cameras [8]. Together these technologies open up a wide field of possibilities to sensitively probe the presence of atoms in crystals.

Imaging as well as chemical mapping of crystalline matter with STEM at atomic resolution require an alignment of the sample along specific crystallographic orientations with respect to the electron beam. This condition, unfortunately, complicates a quantitative compositional analysis. While dynamical diffraction effects can concentrate Bloch waves on certain atomic planes, de-channelling and delocalization also lead to erroneous EXDS and EELS intensities when electrons travel through the material [9–14]. Previous publications e.g. on $SrTiO_3$, InGaAs [15,16,17] and other materials have shown the influence of these channelling effects and provide solutions to overcome the problem, such as atom-counting via statistical analyses [18,19] or simulating scattering phenomena in bulk systems [14,20].

Quantitative analyses in single-phased materials at the atomic scale are challenging; even more so if the elements are not homogenously distributed and occupy preferred sites. Studies on the elemental distribution in bi-layered perovskite-like materials e.g. of Mn and Fe in the brownmillerite $Ca_2Fe_{1.07}Mn_{0.93}O_5$ [21] or La and Sr in the Ruddlesden-Popper phases $La_{2-2x}Sr_{1+2x}Mn_2O_7$ (LSMO) [22–25] impressively demonstrate the possibilities of EELS elemental mapping which is used to determine the elemental ratios in the different layers.

* Corresponding author.
E-mail address: judith.lammer@tugraz.at (J. Lammer).

https://doi.org/10.1016/j.ultramic.2022.113477
Received 9 August 2021; Received in revised form 13 January 2022; Accepted 24 January 2022
Available online 26 January 2022

Already indicated in the data shown in the work on LSMO by *Roldan* et al. [25] is the fact that elements do not only have preferred sites in layered structures, but also seem to vary in their occupation from atomic column to atomic column. With this work, we address this point and introduce a quantification method especially designed for the case where the elemental ratios strongly vary from atomic column to atomic column. As a model system, we used a material from the class of lanthanum barium ferrates with similar crystal structure as used by *Roldan* et al. [25].

The method is based on high-resolution EELS elemental maps and simulations to quantify the chemical composition column-by-column. In our specific case, the atomic columns are occupied by two elements – Ba and La –, which are neighbours in the periodic table. Furthermore, we are able to carry out the final quantification step without using explicit (calculated) ionization cross sections, which is usually mandatory, when performing EELS quantification [26].

2. The material

Ruddlesden-Popper (RP) phases possess good electronic conductivity and high catalytic activity for oxygen reduction combined with a certain tendency for proton/water uptake. Therefore, they are of great interest as possible new materials for future applications in oxygen-ionic or protonic ceramic fuel cells (SOFCs, PCFCs) and electrolyser cells (SOECs, PCECs), or membranes for hydrogen separation [27]. RP-phases are layered materials with alternating perovskite layers and rock salt layers. They commonly show a variation in their oxygen content (described as oxygen nonstoichiometry δ) within the (A,A')O layers of the perovskite block or in the rock salt type $(A,AO)_2$ double layer, which leads to oxygen-ionic conductivity. This double layer structure is further flexible enough for the incorporation of hydroxide (OH^-) or molecular water species [28,29]. Increasing the lattice volume and the lattice parameters weakens the metal-oxygen bonding, and – consequently – increases the oxygen mobility [27]. However, technologies based on these materials are still far from commercialization, which is mainly due to a research deficit in the fields of fundamental structural characterization, mass- and charge transport properties, as well as defect chemistry and their combination, resulting in structure property relations.

The oxide ceramic $Ba_{1.1}La_{1.9}Fe_2O_7$ – a second order Ruddlesden-Popper phase with the general formula $A_3B_2O_7$ – is one of these promising new multi-layered materials with only roughly known crystal structure: Ba and La occupy the A-sites, whereas Fe is located on the B-sites (see Fig. 1).

Previous work on the similar compound $Ba_1La_2Fe_2O_7$ using neutron powder diffraction revealed a non-uniform La/Ba-distribution on the A-sites between rock salt layers and perovskite layers [30,31,32,33]. So far, it has been unknown, if changes in the amount of Ba or La lead to alterations in this distribution, in lattice parameters and in unit cell volume.

3. Experimental methods

3.1. STEM analysis

A TEM lamella was prepared from the sintered $Ba_{1.1}La_{1.9}Fe_2O_7$ sample using a FIB/SEM dual beam microscope FEI NOVA200 NanoLab (Ga-ions, operated at 30 kV; for the final cleaning step we used 5 kV, 70 pA and a tilt angle of 6° and 7°) and it was mounted on an Omniprobe Cu

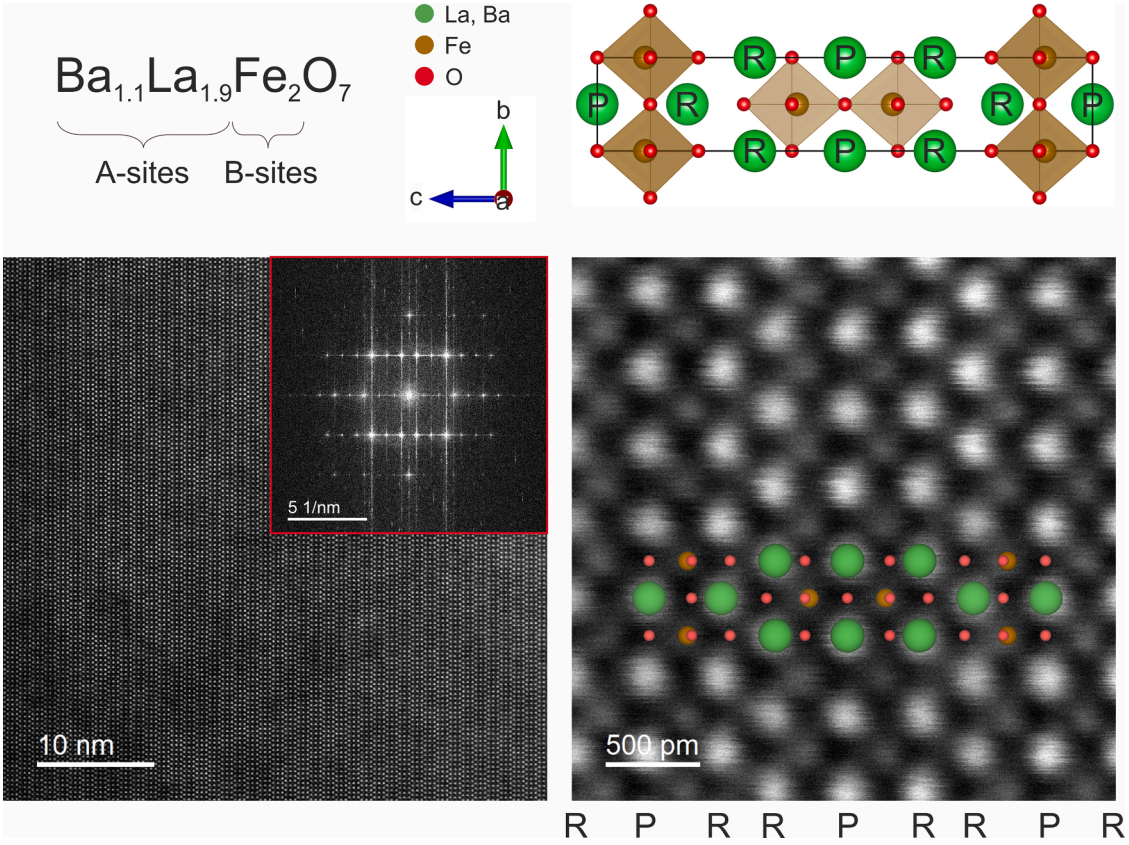

Fig. 1. Top: Crystal structure (unit cell) of $Ba_{1.1}La_{1.9}Fe_2O_7$ in [1 0 0] zone axis. Regions with Fe octahedra belong to the perovskite layer and regions without octahedra are part of the rock salt layer. The A-sites are marked with the letters R and P to indicate whether they belong to the rock salt (R) or to the perovskite (P) layer. Bottom: High-resolution HAADF image with FFT of $Ba_{1.1}La_{1.9}Fe_2O_7$ in [1 0 0] zone axis (left) and close up with superimposed unit cell (right). Columns filled with Ba and La appear brighter, whereas columns with Fe show up darker (O is not visible). Columns in vertical lines belong to the same layer and are marked with R for rock salt and P for perovskite layers.

grid. The high-resolution analyses were performed in STEM mode (nanoprobe mode) on a C_s probe corrected FEI Titan^3 G2 60–300 microscope equipped with a GIF Quantum ERS from Gatan including a K2 Summit direct electron detection camera (EELS). During EEL spectrum image acquisition, we used 300 kV acceleration voltage, approx. 150 pA beam current, 19.6 mrad convergence semi-angle and a 37.7 mrad EELS collection semi-angle. Images and elemental maps were taken from an area with a relative thickness of 0.5 in units of inelastic mean free path, which corresponds to a sample thickness of approximately 50 nm. We worked with GMS 3 (version 3.23) by Gatan to acquire EEL spectrum images using a pixel dwell time of 10 ms.

The chemical information was obtained from raw spectra. For the analysis we applied the integrated model based least square fitting routine using a power-law for the background fit and Hartree-Slater cross section models for the edge shapes. We included the O K, Fe L_{23} as well as the Ba M_{45} and La M_{45} edges in the fit. Since the Fe L_{23}, the Ba M_{45} and La M_{45} edge are close, we decided to link the fitting models for the three elements (fitting ranges were 400 – 667 eV for O K and 570 – 1010 eV for the combined fit of the other three elements). Excluding ELNES and thereby the white lines, the energy window for the La M_{45} intensity was set to a width of 207 eV and 146 eV for Ba M_{45}, respectively.

The column positions in the EELS maps were determined by searching for local intensity maxima in the simultaneously acquired ADF reference. The peak positions were subsequently used as a basis for a Voronoi tessellation. Based on the resulting cells we determined the absolute intensity from the EELS elemental maps, integrated over a defined area corresponding to each atomic column (containing 22 to 29 pixels), while excluding columns not located in the image entirely. This approach is inspired by similar techniques which were successfully applied to high-resolution STEM ADF data [34,35], and proved to be insensitive to slight defocus variations and aberrations [36]. The data evaluation steps were performed using a Matlab script written in MathWorks Inc. Matlab (version R2020).

3.2. X-ray diffraction

XRD measurements of the calcined $Ba_{1.1}La_{1.9}Fe_2O$ powder were performed with a diffractometer (BRUKER-AXS D8 Advance ECO) using a Cu Kα radiation source (1.5418 Å) operated at 40 kV and 25 mA. The diffractogram was recorded at a scanning rate of 0.01° s^{-1}. Lattice parameters were obtained from fitting the peak positions to a tetragonal unit cell (SG: I4/mmm). Rietveld refinement was performed by using the commercially available software TOPAS (Bruker) [37,38]. Reflection broadening was described by the convolution of a Voigt function with a modified pseudo Voigt function according to Thompson–Cox–Hastings [39].

4. Simulations

Zone axis-conditions, the effects of elastic and thermal scattering and the delocalization of the particular ionization edge can produce apparent EELS signals either larger or smaller than the nominal values. To evaluate the amount and approximate composition of the contributions from neighbouring atomic columns (off-axis signal) we simulated the EELS signal using inelastic multislice calculations based on Slater-type orbitals [40–43] (in [1 0 0] zone axis and in accordance with the experimental parameters). The beam was focused on the top surface of the sample. Elastic scattering was taken into account both before and after each inelastic scattering event.

Contributions from on-axis atoms (i.e., at the beam position) and off-axis atoms (i.e., in nearest-neighbour or next-nearest-neighbour columns) were evaluated separately in all cases. Counting the on-axis atoms necessitates the (approximate) removal of any non-local, off-axis contribution (the amount of artefact intensity caused by the electron scattering processes) from the experimental signal. In order to gauge these contributions on the elastic scattering, we simulated three cases with different amounts of Ba and La at the A-sites: two, where we filled all A-sites within the crystal either with Ba or La ($Ba_3Fe_2O_7$ and $La_3Fe_2O_7$), and one, where we filled the A-sites in the perovskite layer with Ba and those in the rock salt layer with La ($BaLa_2Fe_2O_7$). For these configurations we simulated the intensities of the Ba M_{45} (781 eV) and the La M_{45} (832 eV) edges. In this manner, we were able to compare the origin of the signal from both elements and distinguish the behaviour between A-positions in the perovskite layer and in the rock salt layer of the structure.

Since Ba and La differ by only about 2% in nuclear charge and 1% in mass, we expected both atomic species to have similar elastic scattering behaviour, resulting in virtually identical relative off-axis intensity contributions. However, due to the different inelastic scattering probabilities of the Ba M_{45} and the La M_{45} edge, the simulated intensity values of the Ba and the La case cannot be compared directly. Therefore, we calculated the off-axis to on-axis intensity ratios, as for those, all edge-specific factors cancel out. The values are given in Table 1 and show almost no dependency on the type of atom (Ba or La) or the position within the A-sites (perovskite or rock salt layer).

To investigate the influence of elastic scattering in a more realistic (i.e., less homogeneous) system, we performed calculations with $BaLa_2Fe_2O_7$. The simulations (see Fig. 2) reveal the origin of the signal intensities for both the Ba M_{45} edge (top) and the La M_{45} edge (bottom) when placing the beam either on the perovskite layer (marked in grey) or on the rock salt layer (marked in yellow).

The simulations clearly show that the majority of the signal originates from the on-column atoms. With increasing thickness, more and more neighbouring columns start to contribute as the beam broadens and de-channelling effects become more prominent. For the sample thickness used in this study (50 nm), many surrounding atomic columns up to about 1.5 nm from the beam position still have small, but non-negligible contributions. Due to this large beam spread and many contributing atomic columns, the off-axis signal essentially corresponds to an average over a large sample area. To quantify this, we performed extensive calculations in which we scanned the beam over the entire unit-cell with a step-size of about 0.05 nm (corresponding to the experimental step-size) to compute the total Ba M_{45} and La M_{45} intensities averaged over the entire unit-cell. The results collected in Table 2 show that the ratio between the off-axis signal and the intensity averaged over the unit-cell is fairly independent of the investigated atomic column and excitation edge. It varies between 15.78% and 20.77%. The off-axis intensity is slightly higher for columns not containing the element responsible for the excitation edge. However, this variation is small compared to the overall intensity and compared to the experimental uncertainty.

This means, that – in this case – it is possible to introduce a simple channelling correction mechanism for the experimental data by just subtracting a certain amount of the average-unit-cell-intensity from the measured data.

Note that this correction is valid for a certain sample thickness and cannot be applied in general. Our simulations show that geometrical arguments serve as rough estimate for beam broadening at convergence

Table 1
Simulated intensities from Ba and La on A-positions in $Ba_3Fe_2O_7$ and $La_3Fe_2O_7$.

	on-axis intensity [arb.u.]	off-axis intensity [arb.u.]	off-axis to on-axis intensity ratio
La M_{45} in $La_3Fe_2O_7$:			
perovskite layer	337 480	28 436	8.43%
rock salt layer	332 218	27 938	8.41%
Ba M_{45} in $Ba_3Fe_2O_7$:			
perovskite layer	266 637	23 481	8.81%
rock salt layer	262 655	23 262	8.86%

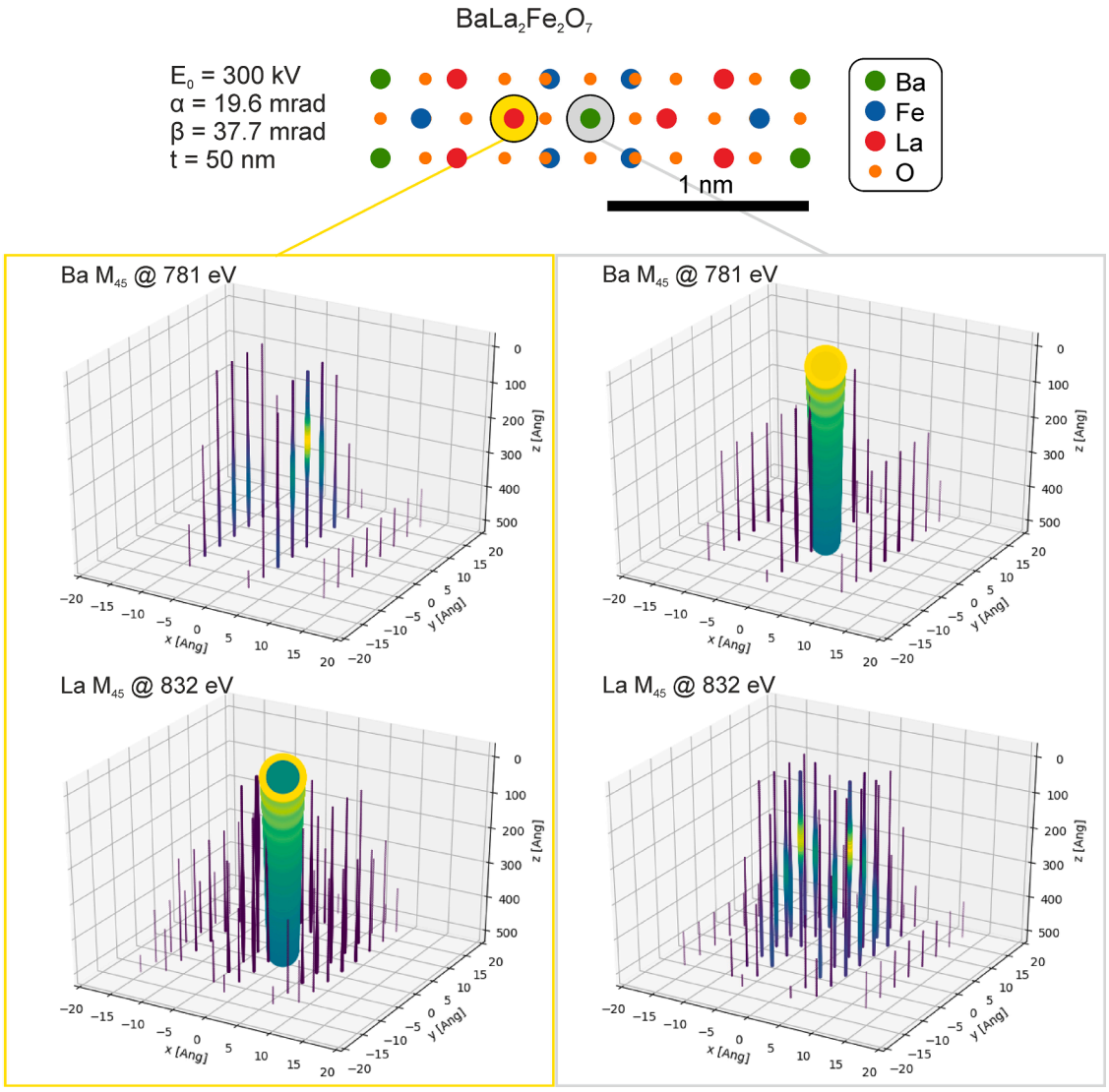

Fig. 2. Inelastic multislice calculations for $BaLa_2Fe_2O_7$: the Ba M_{45} edge and the La M_{45} edge for two beam positions – on the rock salt layer (yellow) and on the perovskite layer (grey). Contributions to the signal (accumulated in z-direction through the sample) do not only stem from the beam position (x = 0, y = 0) but also from the surrounding atomic columns. Values are given in Table 2.

Table 2
Simulated intensities from Ba and La on A-positions in $BaLa_2Fe_2O_7$ including average intensities over the unit cell.

$BaLa_2Fe_2O_7$	on-axis intensity [arb.u.]	off-axis intensity [arb.u.]	unit cell average [arb.u.]	off-axis to unit-cell-average ratio
Ba M_{45}:			40 953	
perovskite layer	266 517	6 463		15.78%
rock salt layer	0	8 506		20.77%
La M_{45}:			101 564	
perovskite layer	0	20 621		20.30%
rock salt layer	332 290	17 628		17.36%

angles typically used in high-resolution STEM: In the following, a brief back of the envelope calculation shall help estimating the thickness regime, where this ansatz works. In our case a convergence semi-angle of approx. 20 mrad and a sample thickness of 50 nm lead to a maximum beam radius of roughly r = 1 nm (using r = t • α for small convergence angles α). In order to use an averaged intensity value for the correction, the beam radius should be larger than (or at least equal to) the distances between the relevant atomic columns (in our case roughly half a unit cell including perovskite and rock salt layers). In cases where r equals approximately one unit cell length, we advise to support the correction with simulations: the beam spreads with ongoing transmission and therefore the contributing off-axis signal will be strongly localised at the point, where the beam enters the sample. Additionally, one has to consider the maximum error tolerance, when averaging over the whole unit cell. In our case variations of the “off-axis to unit-cell-average ratios" between 15% and 20% are acceptable, but that is not necessarily true for other materials (i.e. experiments).

5. Theoretical considerations

In the following, we consider the crystallographic A-site only. Within small areas and constant sample thickness, the number of ions per atomic column is deemed unaltered.

Scattering effects are taken into account by using the results from the simulations described in Chapter 4: According to Table 1, beam spreading conditions for both Ba and La are considered to be equal.

Additionally, we assume, that Ba and La are homogeneously distributed within one column, such that the beam spreading equally affects both elements. Table 2 shows that – because of off-axis contributions from large areas and within a reasonable uncertainty – it is possible to use a distinct amount of the average unit cell intensity as a measure in order to correct for channelling effects in the experimental data.

Therefore, we calculated a mean value for the off-axis to unit-cell-average ratio from Table 2 for Ba and La from both rock salt and perovskite layers (18.3% for Ba and 18.8% for La) and subtracted these amounts of the average unit cell intensity from the experimentally determined signals of the atomic column of interest:

$$I_{Ba} = I_{Ba}^{exp} - 0.183 \cdot I_{\varnothing Ba} \quad (1)$$

$$I_{La} = I_{La}^{exp} - 0.188 \cdot I_{\varnothing La} \quad (2)$$

with

I_x: corrected net intensity of the ionization edge
I_x^{exp}: experimentally determined intensity of the ionization edge (including off-axis signal)
$I_{\varnothing x}$: intensity of the ionization edge averaged over the unit cell (on-axis plus off-axis)

The crystal sites in the atomic columns of interest are occupied by either Ba or La. Hence, one can show that the corrected EELS signals of Ba and La (I_{Ba} and I_{La}) depend on each other linearly (see supplementary information). Using this linearity, one can display and evaluate the Ba and La intensity of several atomic columns from high-resolution EELS elemental maps using a scatter plot [44], where the La intensity of each atomic column is plotted on the abscissa and the Ba intensity on the ordinate. Depending on the amount of Ba and La ions within each column, the measured combinations of Ba and La intensities appear as points on a straight line.

The intercepts of the line with the x- and y-axis correspond to the correlation parameters α_x describing the correlation between the EELS intensity and the concentration:

$$\alpha_x = (n_{Ba} + n_{La})\, I_0 \sigma_x \quad (3)$$

with

n_x: number of atoms per unit area of element x
I_0: incident intensity
σ_x: ionization cross section of element x

The real concentrations are calculated via dividing the corrected intensities by the correlation parameters α_x (see supplementary information). Therefore, the Ba and La column occupancies can be directly extracted from the scatter plot (as illustrated in Chapter 6 in Fig. 4).

This linearity provides a list of helpful features compared to a standard EELS quantification:

- The linearity immediately reveals statistical outliers and provides a simple method to test the quality of the experimentally determined values.
- An intrinsic statistic evaluation is introduced by using the intensities from all atomic columns together for the quantification.
- Even though – in this case – theoretical ionization cross sections were necessary for simulations and net intensities, they are not necessary for the quantification step itself.

6. Results and discussion

EELS elemental maps as displayed in Fig. 3a clearly show La preferring positions in the perovskite layers, whereas Ba mainly

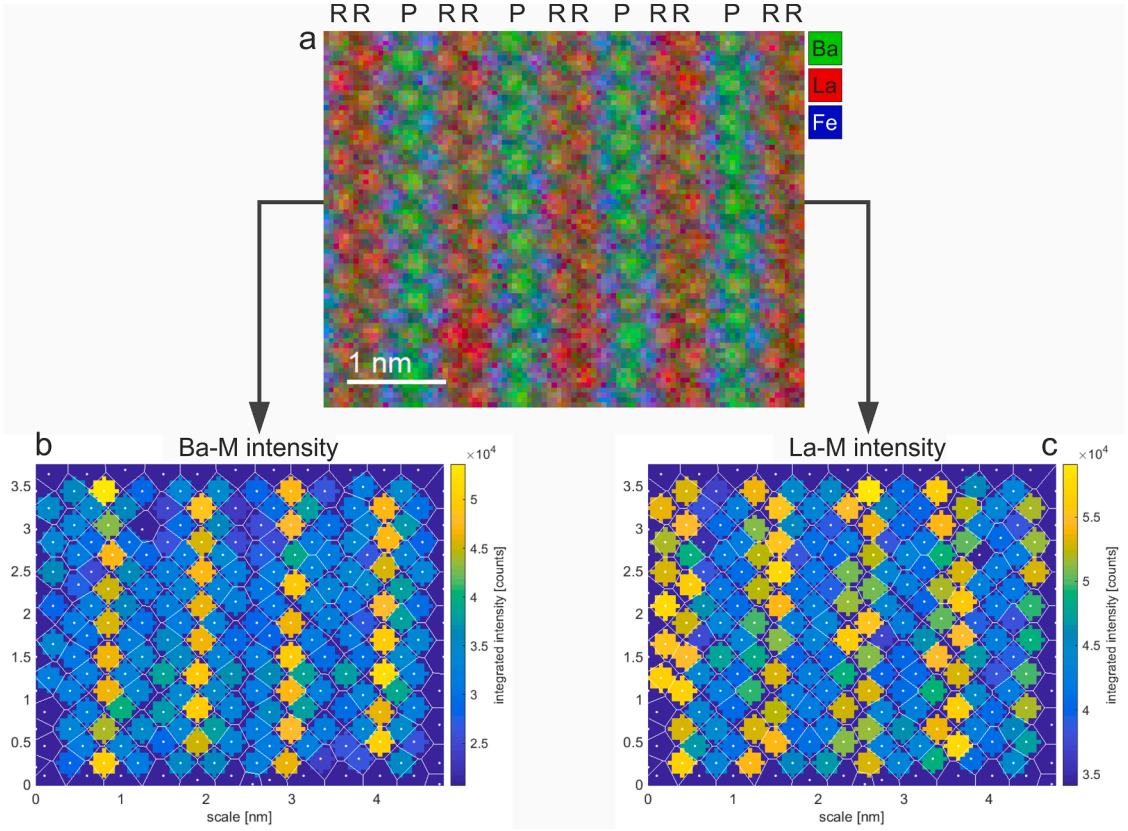

Fig. 3. (a) EELS elemental map RGB overlay of Ba (green), La (red) and Fe (blue) of $Ba_{1.1}La_{1.9}Fe_2O_7$ in [1 0 0] zone axis. Rock salt layers (R) and perovskite layers (P) are marked. (b) and (c) integrated intensities on each atomic column of Ba (b) and La (c).

occupies the rock salt layers. The graphic output of the intensity integration per atomic column shown in Fig. 3b and 3c points out that not all atomic columns exhibit the same intensities (represented by colour) within identical crystal sites. This implies that Ba and La strongly vary within the rock salt layers and the perovskite layers.

The mean net Ba M_{45} and La M_{45} intensity per atomic column after off-axis signal correction according to Eqs. 1 and 2 are plotted as a scatter plot in Fig. 4a. The experimentally determined values show the predicted linear behaviour. In accordance to Fig. 3, the graph displays distinct clusters corresponding to the perovskite layers and the rock salt layers. The scatter of the data points confirms that the chemical composition is not the same on every perovskite- or rock salt position.

Each atomic column can now be quantified using the correlation parameters α_x (see Fig. 4b): for Ba, the concentration in the rock salt layer varies from 20 at% to 35 at% and from 39 at% to 52 at% within the perovskite layer. The mean Ba and La concentrations within both layers are 28 ± 3 at% / 72 ± 4 at% (rock salt layers) and 46 ± 3 at% / 54 ± 3 at % (perovskite layers).

Contrary to characterization techniques like XRD or neutron scattering, analytical methods in STEM render a locally resolved chemical analysis possible: thus, we are not only able to show differences in rock salt layers and perovskite layers of the material, but also give detailed information on variations of Ba and La on equal crystallographic sites. This spectroscopic method also works when observing elements with neighbouring atomic number, while other high-resolution STEM techniques such as counting atoms via Z-contrast reach their limits, since the

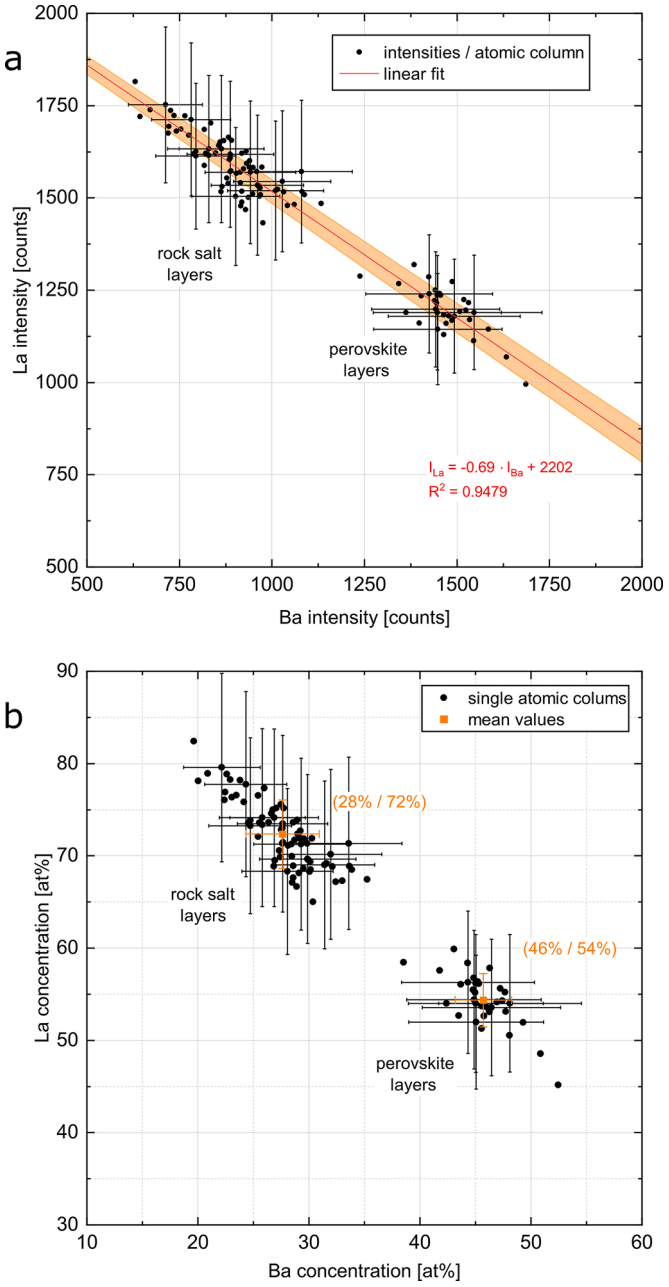

Fig. 4. Scatter plots: (a) La vs. Ba intensities (after correcting for channelling effects) from single atomic columns in the perovskite and the rock salt layers of $Ba_{1.1}La_{1.9}Fe_2O_7$ and linear fit (red line) with orange error bands (±σ for k and d of the fit). (b) La and Ba compositions for each atomic column as well as mean values (orange) for rock salt and perovskite layers. Both figures include black error bars on every sixth data point to illustrate the extend of the maximum error. Orange error bars in (b) display the standard deviation for the mean values.

difference in scattering cross sections resulting from HAADF images is too small [45].

This method benefits from the significant concentration variation from column to column and improves with rising disorder since the correlation parameters of the linear fits become more reliable.

To get an estimate of the quality of this method, we performed an error analysis. The errors of the EELS intensities from the Ba M_{45} and La M_{45} edges were assumed to be 10% (as given in the software GMS 3 for the model based intensity measurement). Since the simulations show that off-axis intensities differ slightly between perovskite layers and rock salt layers, we expect these differences also to be the main source of error in our correction in Eqs. 1 and 2 (2.5% (Ba) and 1.5% (La) of the mean unit-cell intensity). For the correlation parameters α_{Ba} and α_{La} obtained from the linear regression (from Fig. 4a), we used the regression standard errors. Finally, we calculated maximum errors for the intensities and concentrations indicated in Fig. 4.

Several criteria speak for the quality of these results:

The linear regression (red line in Fig. 4a) yields proportionality factors α_x for Ba and La, corresponding to the intercepts of the straight line: $\alpha_{Ba} = 3214 \pm 49$ and $\alpha_{La} = 2202 \pm 17$. To get an estimate on the quality of these factors we compared their ratio to the ratio of calculated Hartree-Slater cross sections σ_x taken from our data evaluation in GMS 3: The results $\alpha_{Ba}/\alpha_{La} = 1.46$ and $\sigma_{Ba}/\sigma_{La} = 1.53$ agree well. Also, the chemical formula calculated from both mean layer concentration values is $Ba_{1.01\pm0,14}La_{1.99\pm0,14}Fe_2O_7$, which is very close to the nominal composition $Ba_{1.1}La_{1.9}Fe_2O_7$ obtained by using the stoichiometric amounts of the cations during the synthesis. Slight local variations in the Ba/La ratio at the same scale were also found in EDXS measurements (out of zone-axis) on several grains of the lamella, which support the reliability of our findings. Furthermore, the maximum errors for individual atomic columns – indicated by the error bars in Fig. 4 – imply large values. However – displaying the linear dependency of both Ba and La intensities – the deviation from a straight line over all atomic columns is much smaller and can be used as an indicator for the quality of the measurement.

Our results exhibit the same tendency as shown in the neutron scattering work for $BaLa_2Fe_2O_7$ by *Gurusinghe et al.* [30], who found concentration ratios for Ba/La of 14% / 86% (rock salt layers) and 73% / 27% (perovskite layers). They argue that this element separation stems from differences in cation radii: smaller lanthanide ions prefer the smaller nine-coordinate sites in the rock salt layers whereas the larger alkaline earth metal ions favour the larger twelve-coordinate sites in the perovskite blocks [30].

In addition, our result may improve XRD measurements by adding

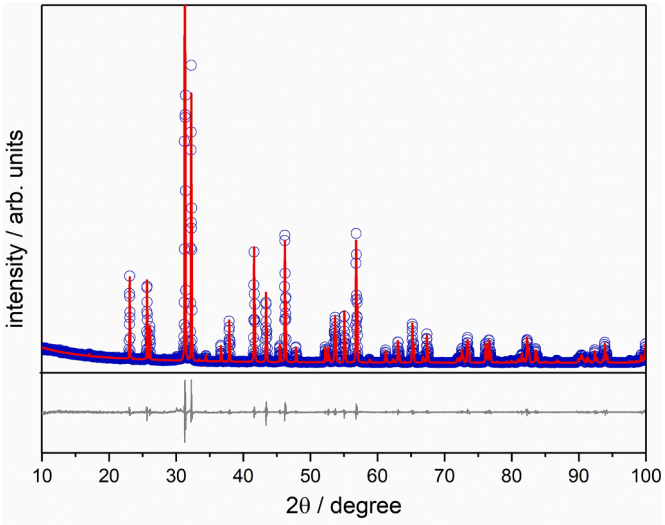

Site	x	y	z	Occupancy	B_{iso} / Å^2
La1	0	0	1/2	0.54	0.30(6)
La2	0	0	0.3181(6)	0.72	0.30(8)
Ba1	0	0	1/2	0.46	0.30(6)
Ba2	0	0	0.3181(6)	0.28	0.30(8)
Fe1	0	0	0.0959(3)	1	0.32(4)
O1	0	0	0	1	0.20(4)
O2	0	0	0.1980(4)	1	0.58(2)
O3	0	1/2	0.1030(2)	1	0.50(4)

a = b / Å	c / Å	V / Å^3
3.929365(17)	20.85765(17)	322.040(4)

Fig. 5. Room temperature XRD pattern of $La_{1.9}Ba_{1.1}Fe_2O_7$ (circles) and fit obtained from Rietveld refinement (red line); the grey line represents the difference plot between measured and calculated data. The fit quality is indicated by the reliability parameters $R_{exp} = 5.59$, $R_{wp} = 12.54$, and $\chi^2 = 2.24$. Atomic positions, site occupancy (taken from the EELS quantification and used as prior information for the Rietveld refinement) and isotropic displacement parameters as well as lattice parameters and unit cell volume of $La_{1.9}Ba_{1.1}Fe_2O_7$ are listed below. Standard deviations (referring to the last or last two digits) are given in parentheses. Atomic positions of Ba were fixed to those of La.

information about site occupancies, which cannot directly be obtained for La and Ba by XRD. Therefore, the EELS quantification results were fed as prior information to the Rietveld refinement performed on the XRD data (see Fig. 5). All detected reflections were assigned to the tetragonal space group I4/mmm (SG #139). The diffractogram matched well with the previously reported isostructural compound $Sr_3Fe_2O_{7-\delta}$ [28]. The lattice parameters and the atomic positions accord accurately with the results published by *Gurusinghe et al.* [30]. Comparing $Ba_1La_2Fe_2O_7$ to $Ba_{1.1}La_{1.9}Fe_2O_7$, equivalent lattice parameters and unit cell volumes but different Ba/La occupancies for both layers strongly imply that the Ba and La distribution in the crystal is driven by the attempt to keep the unit cell volume stable.

7. Summary and conclusions

We introduced a column-by-column quantitative method using EELS in STEM suitable for materials with two elements within the same atomic column - especially with (but not limited to) similar atomic numbers – and with inhomogeneous composition at the nanoscale.

As a model system, we used the second order Ruddlesden-Popper phase $Ba_{1.1}La_{1.9}Fe_2O_7$ and quantified the inhomogeneous distribution of Ba and La within the A-sites. We provide distinct information on the element occupancy distribution within the layers in the material: in this case, the La / Ba concentration strongly varies between the rock salt layer and the perovskite block and – moreover – up to 15 percentage points in atomic columns within the same crystallographic sites.

The chemical information obtained with this quantification method may furthermore be used to improve results obtained with other techniques, e.g. the crystallographic parameters from XRD and Rietveld refinement. Combining the result from XRD and EELS quantification renders the linkage of ordering phenomena in multi-layered materials to their unit cell volume possible.

Measuring in zone-axis usually comes with de-channelling effects depending on the sample thickness. Consequently, inelastic multislice simulations were performed in order to analyse the beam spreading and correct the data for additional off-axis signal. In our case similar element masses as well as a similar crystallographic surrounding result in an almost identical channelling behaviour for both elements. The sample thickness of 50 nm causes the beam to spread to a radius of approximately half a unit cell, which then causes the *off-axis to unit-cell-average intensity ratio* to be relatively stable over all A-sites. This enables us to perform a simple correction via subtracting a certain percentage of the mean unit cell intensity from the signal.

The method is based on the fact that the La and Ba intensities follow a linear behaviour according to their occupation ratio in each atomic column. Harnessing this correlation automatically introduces an intrinsic statistic evaluation, provides information on the quality of the data and in principle allows to quantify without theoretical scattering cross sections – presupposed they are not needed for obtaining the edge intensities or simulations.

As a final comment, we want to mention, that this column-by-column quantification method to uncover strong concentration variations at the atomic scale is not limited to EELS but may also be applied to high-resolution EDXS.

Funding sources

This work was supported by the Austrian Research Promotion Agency FFG [grant No. 853538], the Klima- und Energiefonds within the program 'Energieforschung (e!MISSION)' [grant No. 871659], the European Union Horizon 2020 programme [grant No. 823717–ESTEEM3] and the Austrian Science Fund FWF [grant No. I4309-N36]. The authors acknowledge financial support by the 'Zukunftsfonds Steiermark' for the purchase of the K2-camera through the 'ASTEM upgrade' project (grant No. 9016).

Declaration of Competing Interest

During data acquisition and data evaluation of this work Paolo Longo worked as employee of Gatan, Inc.; they developed and are marketing the EELS spectrometer and K2 camera used in this work. The other authors declare no competing interests.

Acknowledgement

The authors acknowledge Mr. Sebastian Rauch, who prepared the FIB lamella. JL and CB thank Dr. Rotraut Merkle for fruitful discussions on cation diffusion in oxide ceramics.

Supplementary materials

Supplementary material associated with this article can be found, in the online version, at doi:10.1016/j.molstruc.2021.131573.

References

[1] O.L. Krivanek, N. Dellby, A.J. Spence, R.A. Camps, L.M. Brown, Aberration correction in the STEM, Inst. Phys. Conf. Ser. EMAG97 (1997) 35–40.
[2] P.E. Batson, N. Dellby, O.L. Krivanek, Sub-ångstrom resolution using aberration corrected electron optics, Nature 418 (2002) 617–620, https://doi.org/10.1038/nature00972.
[3] M. Haider, H. Rose, S. Uhlemann, E. Schwan, B. Kabius, K. Urban, A spherical-aberration-corrected 200kV transmission electron microscope, Ultramicroscopy 75 (1998) 53–60, https://doi.org/10.1016/S0304-3991(98)00048-5.
[4] M. Haider, S. Uhlemann, E. Schwan, H. Rose, B. Kabius, K. Urban, Electron microscopy image enhanced, Nature 392 (1998) 768–769, https://doi.org/10.1038/33823.
[5] H. Rose, Outline of a spherically corrected semi-aplanatic medium-voltage TEM, Optik 85 (1990) 19–24.
[6] P. Lechner, S. Eckbauer, R. Hartmann, S. Krisch, D. Hauff, R. Richter, H. Soltau, L. Strüder, C. Fiorini, E. Gatti, A. Longoni, M. Sampietro, Silicon drift detectors for high resolution room temperature X-ray spectroscopy, Nucl. Instrument. Method. Phys. Res. Sect. A 377 (1996) 346–351, https://doi.org/10.1016/0168-9002(96)00210-0.
[7] H.v. Harrach, P. Dona, B. Freitag, H. Soltau, A. Niculae, M. Rohde, An integrated silicon drift detector system for FEI Schottky field emission transmission electron microscopes, Microscopy Microanal. 15 (2009) 208–209, https://doi.org/10.1017/S1431927609094288.
[8] J.L. Hart, A.C. Lang, A.C. Leff, P. Longo, C. Trevor, R.D. Twesten, M.L. Taheri, Direct detection electron energy-loss spectroscopy: a method to push the limits of resolution and sensitivity, Scientific Reports 7 (2017) 8243, https://doi.org/10.1038/s41598-017-07709-4.
[9] J. Taftø, G. Lehmpfuhl, Direction dependence in electron energy loss spectroscopy from single crystals, Ultramicroscopy 7 (1982) 287–294, https://doi.org/10.1016/0304-3991(82)90176-0.
[10] M. Watanabe, D.W. Ackland, A. Burrows, C.J. Kiely, D.B. Williams, O.L. Krivanek, N. Dellby, M.F. Murfitt, Z. Szilagyi, Improvements in the X-ray analytical capabilities of a scanning transmission electron microscope by spherical-aberration correction, Microscopy Microanal. 12 (2006) 515–526, https://doi.org/10.1017/S1431927606060703.
[11] F. Meisenkothen, R. Wheeler, M.D. Uchic, R.D. Kerns, F.J. Scheltens, Electron channeling: a problem for x-ray microanalysis in materials science, Microscopy Microanal. 15 (2009) 83–92, https://doi.org/10.1017/S1431927609090242.
[12] N.R. Lugg, M. Haruta, M.J. Neish, S.D. Findlay, T. Mizoguchi, K. Kimoto, L.J. Allen, Removing the effects of elastic and thermal scattering from electron energy-loss spectroscopic data, Appl. Phys. Lett. 101 (2012), 183112, https://doi.org/10.1063/1.4765657.
[13] B.D. Forbes, A.J. D'Alfonso, R.E.A. Williams, R. Srinivasan, H.L. Fraser, D. W. McComb, B. Freitag, D.O. Klenov, L.J. Allen, Contribution of thermally scattered electrons to atomic resolution elemental maps, Phys. Rev. B 86 (2012), https://doi.org/10.1103/PhysRevB.86.024108.
[14] K.E. MacArthur, H.G. Brown, S.D. Findlay, L.J. Allen, Probing the effect of electron channelling on atomic resolution energy dispersive X-ray quantification, Ultramicroscopy 182 (2017) 264–275, https://doi.org/10.1016/j.ultramic.2017.07.020.
[15] A.J. D'Alfonso, B. Freitag, D. Klenov, L.J. Allen, Atomic-resolution chemical mapping using energy-dispersive x-ray spectroscopy, Phys. Rev. B 81 (2010), https://doi.org/10.1103/PhysRevB.81.100101.
[16] M.-W. Chu, S.C. Liou, C.-P. Chang, F.-S. Choa, C.H. Chen, Emergent chemical mapping at atomic-column resolution by energy-dispersive x-ray spectroscopy in an aberration-corrected electron microscope, Phys. Rev. Lett. 104 (2010), 196101, https://doi.org/10.1103/PhysRevLett.104.196101.
[17] G. Kothleitner, M.J. Neish, N.R. Lugg, S.D. Findlay, W. Grogger, F. Hofer, L. J. Allen, Quantitative Elemental Mapping at Atomic Resolution Using X-Ray Spectroscopy, Phys. Rev. Lett. 112 (2014), https://doi.org/10.1103/PhysRevLett.112.085501.

[18] S. van Aert, A. de Backer, G.T. Martinez, B. Goris, S. Bals, G. van Tendeloo, A. Rosenauer, Procedure to count atoms with trustworthy single-atom sensitivity, Phys. Rev. B 87 (2013), https://doi.org/10.1103/PhysRevB.87.064107.
[19] A.D. Backer, S. van Aert, P.D. Nellist, L. Jones, Procedure for 3D atomic resolution reconstructions using atom-counting and a Bayesian genetic algorithm.
[20] L.J. Allen, Simulation in elemental mapping using aberration-corrected electron microscopy, Ultramicroscopy 180 (2017) 142–149, https://doi.org/10.1016/j.ultramic.2017.03.001.
[21] M. Haruta, Y. Hosaka, N. Ichikawa, T. Saito, Y. Shimakawa, H. Kurata, Determination of elemental ratio in an atomic column by electron energy loss spectroscopy, ACS nano 10 (2016) 6680–6684, https://doi.org/10.1021/acsnano.6b01887.
[22] K. Kimoto, T. Asaka, T. Nagai, M. Saito, Y. Matsui, K. Ishizuka, Element-selective imaging of atomic columns in a crystal using STEM and EELS, Nature 450 (2007) 702–704, https://doi.org/10.1038/nature06352.
[23] J. Gázquez, G. Sánchez-Santolino, N. Biškup, M.A. Roldán, M. Cabero, S. J. Pennycook, M. Varela, Applications of STEM-EELS to complex oxides, Mater. Sci. Semiconduct. Process. 65 (2017) 49–63, https://doi.org/10.1016/j.mssp.2016.06.005.
[24] P.D. Battle, M.A. Green, N.S. Laskey, J.E. Millburn, L. Murphy, M.J. Rosseinsky, S. P. Sullivan, J.F. Vente, Layered Ruddlesden−popper manganese oxides: synthesis and cation ordering, Chem. Mater. 9 (1997) 552–559, https://doi.org/10.1021/cm960398r.
[25] M.A. Roldan, M.P. Oxley, Q.'a. Li, H. Zheng, K.E. Gray, J.F. Mitchell, S. J. Pennycook, M. Varela, Atomic scale studies of La/Sr ordering in colossal magnetoresistant La(2-2x)Sr(1+2x)Mn2O7 single crystals, Microscopy Microanal. 20 (2014) 1791–1797, https://doi.org/10.1017/S1431927614013075.
[26] R.F. Egerton, Electron Energy-Loss Spectroscopy in the Electron Microscope, Springer US, Boston, MA, 2011.
[27] N. Tarasova, I. Animitsa, A. Galisheva, D. Korona, Incorporation and conduction of protons in Ca, Sr, Ba-Doped BaLaInO4 with Ruddlesden-Popper structure, Materials (Basel, Switzerland) (2019) 12, https://doi.org/10.3390/ma12101668.
[28] M. Matvejeff, M. Lehtimäki, A. Hirasa, Y.-H. Huang, H. Yamauchi, M. Karppinen, New water-containing phase derived from the Sr3Fe2O7-δ Phase of the Ruddlesden−Popper structure, Chem. Mater 17 (2005) 2775–2779, https://doi.org/10.1021/cm050106z.
[29] V. Øygarden, H. Fjellvåg, M.H. Sørby, A.O. Sjåstad, Crystal structure of LaSr3Fe3O8(OH)2•xH2O, Inorganic Chem. 55 (2016) 7630–7636, https://doi.org/10.1021/acs.inorgchem.6b01085.
[30] N.N.M. Gurusinghe, J. de La Figuera, J.F. Marco, M.F. Thomas, F.J. Berry, C. Greaves, Synthesis and characterisation of the n=2 Ruddlesden–Popper phases Ln2Sr(Ba)Fe2O7 (Ln=La, Nd, Eu), Mater. Res. Bull. 48 (2013) 3537–3544, https://doi.org/10.1016/j.materresbull.2013.05.058.
[31] N.N.M. Gurusinghe, J.C. Fones, J.F. Marco, F.J. Berry, C. Greaves, Fluorine Insertion Into the Ruddlesden-Popper phase La2BaFe2O7: the Structure and Magnetic Properties of La2BaFe2O5F4, 43, Dalton transactions (Cambridge, England 2003), 2014, pp. 2038–2043, https://doi.org/10.1039/c3dt52769g.
[32] D. Samaras, A. Collomb, Rotation des moments magnetiques dans BaLa2Fe2O7, Solid State Commun. 16 (1975) 1279–1284, https://doi.org/10.1016/0038-1098(75)90828-5.
[33] J.C. Joubert, D. Samaras, A. Collomb, G.Le Flem, A. Daoudi, Sur quelques nouveaux oxydes mixtes de formule BaLn2Fe2O7 et SrLn2Fe2O7, Mater. Res. Bull. 6 (1971) 341–344, https://doi.org/10.1016/0025-5408(71)90167-X.
[34] L. Jones, K.E. MacArthur, V.T. Fauske, A.T.J. van Helvoort, P.D. Nellist, Rapid estimation of catalyst nanoparticle morphology and atomic-coordination by high-resolution Z-contrast electron microscopy, Nano Lett. 14 (2014) 6336–6341, https://doi.org/10.1021/nl502762m.
[35] D. Knez, G. Dražić, S.K. Chaluvadi, P. Orgiani, S. Fabris, G. Panaccione, G. Rossi, R. Ciancio, Unveiling Oxygen Vacancy Superstructures in Reduced Anatase Thin Films, Nano letters 20 (2020) 6444–6451, https://doi.org/10.1021/acs.nanolett.0c02125.
[36] H. E, K.E. MacArthur, T.J. Pennycook, E. Okunishi, A.J. D'Alfonso, N.R. Lugg, L. J. Allen, P.D. Nellist, Probe integrated scattering cross sections in the analysis of atomic resolution HAADF STEM images, Ultramicroscopy 133 (2013) 109–119, https://doi.org/10.1016/j.ultramic.2013.07.002.
[37] Bruker, Bruker AXS Topas V5: General profile and Structure Analysis Software for Powder Diffraction Data, User's manual, Karlsruhe, Germany, 2014.
[38] A.A. Coelho, TOPAS and TOPAS-Academic an optimization program integrating computer algebra and crystallographic objects written in C++, J. Appl. Crystallogr. 51 (2018) 210–218, https://doi.org/10.1107/S1600576718000183.
[39] P. Thompson, D.E. Cox, J.B. Hastings, Rietveld refinement of Debye–Scherrer synchrotron X-ray data from Al2O3, J. Appl. Crystallogr. 20 (1987) 79–83, https://doi.org/10.1107/S0021889887087090.
[40] E.J. Kirkland, Advanced Computing in Electron Microscopy, 2nd ed, Springer Science+Business Media LLC, Boston, MA, 2010.
[41] P. Schattschneider, M. Nelhiebel, B. Jouffrey, Density matrix of inelastically scattered fast electrons, Phys. Rev. B 59 (1999) 10959–10969, https://doi.org/10.1103/PhysRevB.59.10959.
[42] S. Löffler, V. Motsch, P. Schattschneider, A pure state decomposition approach of the mixed dynamic form factor for mapping atomic orbitals, Ultramicroscopy 131 (2013) 39–45, https://doi.org/10.1016/j.ultramic.2013.03.021.
[43] S. Löffler, P. Schattschneider, Transition probability functions for applications of inelastic electron scattering, Micron (Oxford, England 1993) 43 (2012) 971–977, https://doi.org/10.1016/j.micron.2012.03.020.
[44] W. Grogger, F. Hofer, G. Kothleitner, Quantitative chemical phase analysis of EFTEM elemental maps using scatter diagrams, Micron (Oxford, England 1993) 29 (1998) 43–51, https://doi.org/10.1016/S0968-4328(97)00061-9.
[45] A. de Backer, G.T. Martinez, K.E. MacArthur, L. Jones, A. Béché, P.D. Nellist, S. van Aert, Dose limited reliability of quantitative annular dark field scanning transmission electron microscopy for nano-particle atom-counting, Ultramicroscopy 151 (2015) 56–61, https://doi.org/10.1016/j.ultramic.2014.11.028.